Calculation of cerium and lanthanum anomalies in geological and environmental samples

Jean-Alix J-A Barrat, Germain Bayon, Stefan Lalonde

Calculation of cerium and lanthanum anomalies in geological and environmental samples

by

Jean-Alix Barrat[1,2], Germain Bayon[3] and Stefan Lalonde[3]

[1]Univ Brest, CNRS, LEMAR, Institut Universitaire Européen de la Mer (IUEM), Place Nicolas Copernic, 29280 Plouzané, France. E-Mail: barrat@univ-brest.fr. (corresponding author).

[2]Institut Universitaire de France.

[3]Univ Brest, CNRS, Ifremer, Geo-Ocean, F-29280 Plouzané, France

submitted to *Chemical Geology*, 12/05/2022

Abstract

The determination of La and Ce anomalies in natural waters, biological samples and sedimentary rocks can provide unique information on biogeochemical processes in Earth surface environments. Over the last decades, several approaches have been used for calculating La/La* and Ce/Ce*, based on the comparison between measured and theoretical abundances (La* and Ce*) extrapolated from neighboring rare earth element concentrations normalized to chondritic or shale reference values. These extrapolations can be achieved either linearly or semi-logarithmically ("geometrically"), both methods being used in the literature in the absence of any consensus. We show here, using a database of rocks exhibiting no La and Ce anomaly, that the linear extrapolation of La and Ce abundances can result in markedly different results depending on whether chondritic or shale values are used for normalization. The geometric extrapolation allows consistent calculation of La and Ce anomalies for the entire compositional range tested in this study, regardless of whether data are normalized to chondritic or shale reference values. The differences between linear and geometric extrapolations are illustrated by a few selected examples from the literature, including various carbonate rock and seawater samples, further demonstrating that linear extrapolation can result in erroneous estimates of La and Ce anomalies. We thus propose that La/La* and Ce/Ce* ratios in all geological and environmental samples should be determined using the geometric extrapolation only.

Key words

Rare earth elements, La anomaly, Ce anomaly, linear extrapolation, geometric extrapolation

1/ Introduction

Over the last sixty years, rare earth elements (REE) have become one of the most studied groups of elements in Earth sciences. These elements have the particularity of having an extremely coherent geochemical behavior that can be classically described with the famous "Masuda-Coryell plots" (Masuda, 1962; Coryell et al., 1963), known today as "rare earth patterns". The principle of these diagrams is simple. Rare earth elements are ordered by increasing atomic number, and their abundances in any given sample are normalized to a set of reference values that generally correspond to average concentrations for chondrites (e.g., Anders and Grevesse, 1989; Pourmand et al., 2012; Barrat et al., 2012; Palme et al., 2014) or shales (e.g., Nance and Taylor, 1976; Pourmand et al., 2012; Bau et al., 2018). The first advantage of these diagrams is that the Oddo-Harkins effect (i.e. chemical elements with even atomic numbers are more abundant than adjacent odd atomic number elements) disappears with normalization. Smooth REE patterns are generally obtained for most geological and environmental samples, mostly because all REE are trivalent and not significantly decoupled from each other under relevant physico-chemical conditions. There are notable exceptions, however. For instance, europium (Eu^{2+} and Eu^{3+}) and cerium (Ce^{3+} and Ce^{4+}) can be found in two valence states in geological samples. During particular magmatic or environmental processes, these two elements can be significantly decoupled from their neighboring REE, thereby producing specific elemental depletion or enrichment in normalized REE patterns. Additionally, significant anomalies in La, Sm, Gd and Tm can be also found in terrestrial rocks or natural waters, unrelated to any effect of valence. The occurrence of Tm anomalies in terrestrial rocks are thought to be inherited from the building blocks that formed our planet (Dauphas and Pourmand, 2015; Barrat et al., 2016). The origin of other anomalies is not always well understood, except when they are the result of environmental pollution (e.g., Bau and Dulski, 1996b; Kulaksiz and Bau, 2007, 2013; Merschel and Bau, 2015; Ma et al., 2019; Le Goff et al., 2019, Valdés-Vilchis, 2021).

Among these anomalies, Ce anomalies have received considerable interest. The distinctive behavior of Ce in the marine environment was discovered more than 50 years ago (e.g., Goldberg et al., 1963). The first reliable REE analyses of seawater, various authigenic phases, and ichtyoliths showed very early on that aqueous phases, marine carbonates and other seawater archives could display pronounced negative Ce anomalies (e.g., Piper, 1974; Elderfield and Pagett, 1986 and references therein). The role of Fe and Mn oxides in the development of these anomalies was subsequently proposed because Mn-rich nodules and

crusts displayed complementary positive anomalies in Ce (e.g., Goldberg et al., 1963; Piper, 1974). Today, it is generally well accepted that the decoupling of Ce from other REEs in the oceans, or more generally in aqueous environments, mainly results from oxidative scavenging of Ce by Fe and Mn hydroxides (e.g., Bau and Koschinsky, 2009). The occurrence of Ce anomalies in natural waters and in the biogenic or authigenic phases that precipitate from them is used as a proxy for oxidative conditions in Earth surface environments (e.g., German and Elderfield, 1990; German et al., 1991; Bau et al., 1997; Wallace et al., 2017; Bellefroid et al., 2018). Cerium anomalies are also of interest for magma-related studies, although their application to basalts and other igneous rocks remains limited. Lavas from subduction zones and oceanic islands occasionally show negative Ce anomalies, interpreted as reflecting a recycled sedimentary component in their mantle sources (e.g., Shimizu et al., 1992; Class and Le Roex, 2008). In contrast, zircons frequently show excess Ce (Ce^{4+} having the same ionic radius as Zr^{4+}), indicating preferential selective incorporation of Ce relative to neighboring REE during crystal growth. The resulting positive Ce anomalies could reflect the Ce^{4+}/Ce^{3+} ratios of their parental magmas, and therefore provide constraints on oxygen fugacity (e.g., Burnham and Berry, 2012; Trail et al., 2012; Smythe and Brenan, 2016).

Unlike Ce, the La anomaly in geological and environmental samples has received much less attention. Lanthanum anomalies represent a common feature in seawater and marine authigenic phases (e.g., Elderfield, 1988; Tostevin et al., 2016), but remains to date undocumented in igneous rocks. The cause of these anomalies is still poorly understood but could relate to the higher stability of La in solution relative to the other light REE (De Baar et al., 1985, Byrne and Kim, 1990, Byrne et al., 1996). Previous studies have suggested that marine barite could play a role in the development of La anomalies in seawater (Grenier et al., 2018). Indeed, Hein et al. (2007) have reported positive La anomalies in this phase. It is likely that the La excesses they measured, however, are ~~only~~ analytical artefacts generated in the plasma, notably isobaric interferences from Ba (e.g., $^{138}BaH^{+}$ on $^{139}La^{+}$~~?~~), and need to be confirmed. Recently, a number of pioneering studies have demonstrated that biological activity can also fractionate light-REE (e.g., Pol et al., 2014; Semrau et al., 2018; Bayon et al., 2020a). Wang et al. (2020) reported positive La anomalies in methanotrophic mussels at submarine methane seeps, interpreted as resulting from microbial enzymatic activity related to aerobic methane oxidation. These results ~~have~~ suggest~~ed~~ that the La anomaly could ~~be~~ serve as a diagnostic tool for tracing past biological activity related to aerobic methanotrophy. Moreover, La also represents an emerging pollutant in modern environments due to its widespread

industrial use in ~~the industry~~ in magnetic alloys and ~~or~~ catalysts for gasoline engines (Kulaksiz and Bau, 2013; Merschel and Bau, 2015). The emergence of anthropogenic La issues in Earth surface environments calls for a better understanding of the mechanisms that control the decoupling of La from neighboring REE in aquatic environments.

Over the last few decades, different methods have been proposed for calculating La and Ce anomalies in geological and environmental samples, yet no consensus exists among geochemists on best practices for these calculations. In the literature, historical conventions ~~usages~~ or habits prevail. These anomalies are calculated from normalized concentrations and by interpolating or extrapolating La and Ce concentrations (La* and Ce*) assuming smooth REE patterns with linear or logarithmic scales. This results in anomaly values that can be very different from one study to another~~,~~ and cannot be compared. Here we show that that some commonly used approaches for calculating La and Ce anomalies can lead to aberrant results, hence our call for a standardization of the calculation.

2/ The different ways to calculate La and Ce anomalies

2.1/ Normalization values

The patterns of average CI chondrites and average shales do not show significant anomalies in La and Ce when normalized to each other. Therefore, one would expect to calculate similar La/La* or Ce/Ce* values in any given sample following normalization to either chondritic or shale reference values. We will see below that this is not necessarily the case. In this work, we used the average of the Orgueil chondrite concentrations measured by Barrat et al. (2012), and the Post Archean Australian Shale (PAAS) average obtained by Pourmand et al. (2012), which was recalculated relative to our standard values to correct for a slight calibration bias (Barrat et al., 2020). These preferred normalization values are given in Table 1. In the following, X_{CI} and X_{SN} corresponds to the element X concentrations normalized to chondritic or shales values, respectively.

2.2/ The calculation of Ce and La anomalies

By definition, an anomaly visualized in a normalized-REE diagram for an element (X) can be quantified by dividing its measured abundance by its theoretical concentration in the

absence of any anomaly (X*). This latter can be calculated by interpolation or extrapolation using the normalized abundances of ~~for~~ neighboring elements, assuming a smooth REE pattern. The measured/theoretical ~~ratio~~ elemental ratio (X/X*) thus makes it possible to quantitatively measure a positive (X/X*>1) or a negative (X/X*<1) anomaly for this element.

Many approaches to calculating Ce* and La* have been proposed in the last few decades. In the case of magmatic rocks or zircons, which are devoid of La anomalies, Ce* is given by the geometric mean of the normalized concentrations of La and Pr, or interpolated "semi-logarithmically" between La and Nd when Pr abundances are not determined:

$$Ce/Ce^* = Ce_{CI}/(La_{CI} \times Pr_{CI})^{1/2} \quad (1)$$

or

$$Ce/Ce^* = Ce_{CI}/(La_{CI}^{2/3} \times Nd_{CI}^{1/3}) \quad (2)$$

The choices of a geometric mean or the semi-log interpolation are justified here by the fact that the REE patterns are plotted in semi-log diagrams, where linear abscissa corresponds to the number of protons (Z) of REE and ordinates refer to normalized concentrations conventionally displayed in logarithmic scale.

During the 1970s, new developments in sedimentary geochemistry were accompanied by ~~with~~ increasing use of reference shale values for normalizing measured REE abundances (e.g., Piper, 1974). In these early studies, Ce* was interpolated as described above (e.g., Piper (1974) with Equation 2) but also linearly, ~~hence~~ considering that shale-normalized REE patterns were sometimes plotted using linear scales for both ordinates and abscissae. Additionally, prior to the 1990s and the advent of ICP-MS, REE abundances were mostly measured by INAA and Pr concentrations were rarely determined, meaning that Ce* was generally interpolated between La and Nd (e.g., Elderfield and Greaves, 1981), and occasionally between La and Sm (Toyoda et al., 1990):

$$Ce/Ce^* = 3\ Ce_{SN}/(2\ La_{SN} + Nd_{SN}) \quad (3)$$

$$Ce/Ce^* = 5\ Ce_{SN}/(4\ La_{SN} + Sm_{SN}) \quad (4)$$

It was only with the development of plasma source mass spectrometry in the mid-1980's that the simultaneous determination of the concentrations of all the REE's in ~~the~~ a given sample~~s was greatly facilitated~~ became routine, and the number of analyses that also included~~ing~~ Pr

165 increased considerably. The calculation of the Ce anomaly with Ce* linearly interpolated
166 between La and Pr, is given by the following equation (e.g., De Baar et al., 1983):

167 $$Ce/Ce^* = 2\ Ce_{SN}/(La_{SN} + Pr_{SN}) \quad (5)$$

168 However, many natural waters, biogenic or authigenic precipitates, and sediments
169 display La anomalies, thereby biasing the determination of the Ce anomaly using the above
170 formula. With this approach, the calculation of Ce* calculated with La abundances using either
171 linear or geometrical interpolations (Fig. 1) resulted in biased results, generating for instance
172 Ce/Ce* ratios < 1 even in the case of samples devoid of any Ce anomaly. For this reason, Bau
173 and Dulski (1996a) developed a Ce/Ce* vs. Pr/Pr* diagram (Fig. 2, with Ce* linearly
174 interpolated between La and Pr (equation 5), and Pr* linearly interpolated between Ce and Nd,
175 $Pr^*_{SN}=(Ce_{SN} + Nd_{SN})/2$). This plot can be used to identify whether La anomalies are present or
176 not, and whether Ce/Ce* ratios < 1 correspond to true negative Ce anomalies or not. This
177 diagram, which was also popularized by Webb and Kamber (2000), is frequently used today.
178 We will come back to it later.

179 Since one cannot properly interpolate Ce* using La with Pr or Nd abundances, one can
180 instead extrapolate Ce* and La* with Pr and Nd abundances (Fig. 1). To avoid ambiguity, we
181 use here the symbols X^{*g} and X^{*l} for the geometric (semi-log) and linear extrapolations,
182 respectively, of the theoretical concentrations of X. The following equations give La_{SN}^{*g},
183 Ce_{SN}^{*g}, La_{SN}^{*l}, and Ce_{SN}^{*l} [e.g., Bolhar et al. (2004) for the linear interpolations and Lawrence
184 et al. (2006) for the geometric interpolations], and of course similar equations can be written
185 for the chondritic normalization:

186 $$La_{SN}^{*g} = Pr_{SN}^3/Nd_{SN}^2 \quad (6)$$

187 $$Ce_{SN}^{*g} = Pr_{SN}^2/Nd_{SN} \quad (7)$$

188 $$La_{SN}^{*l} = 3\ Pr_{SN} - 2\ Nd_{SN} \quad (8)$$

189 $$Ce_{SN}^{*l} = 2\ Pr_{SN} - Nd_{SN} \quad (9)$$

190

191 These are the equations used by most teams working today on sedimentary rocks or
192 natural waters, without consensus on whether geometric or linear interpolations should be used
193 or not. Questions arise about whether linear or geometric extrapolation allows for a better

194 estimation of the anomalies. Additionally, do the normalization values (chondrite or shale) lead
195 to different estimates of La and Ce anomalies?

196

197 2.3/ Which type of extrapolation to select?

198 An ideal extrapolation should meet the following criteria:

199 - To allow for the best estimation of La* and Ce* concentrations;

200 - To be universal, i.e. to correctly estimate La* and Ce* over the ~~whole~~ entire compositional
201 range encountered in Earth systems;

202 - To be independent of normalization values; in other words, the type of extrapolation must be
203 able to calculate consistent La/La* or Ce/Ce* ratios even if the data are normalized to chondritic
204 or shale values.

205 We have built a database including a total of 286 magmatic rocks, covering a large range
206 of light-REE depletion or enrichment, in order to evaluate the ~~utility~~ ability of both linear and
207 geometric extrapolations to meet these requirements (Hamelin et al., 2009, 2010; Cordier et al.,
208 2010; Daoud et al., 2010; Pelleter et al., 2014; Barrat et al., 2016; Caroff et al., 2021, Pelleter
209 et al., 2014). The chosen suite of igneous rocks ranges from highly-depleted MORBs to highly-
210 enriched alkaline rocks through lamprophyres, and some evolved rocks [$(La/Sm)_{CI}$ = 0.24 -
211 13.4]. All of these rocks were analyzed using the same procedure and calibration to avoid any
212 potential analytical bias (e.g., Barrat et al., 2012). Finally, and obviously most importantly,
213 these rocks do not have Ce, nor La anomalies: their "correct" La/La* or Ce/Ce* ratios are hence
214 ~1.

215 We calculated the Ce/Ce* ratio with Ce* interpolated geometrically between La and Pr
216 (equation 1) for the rocks in our database. This ratio varies from 0.92 to 1.11 only, with most
217 of the samples exhibiting Ce/Ce* between 0.95 and 1.05, confirming the lack of significant Ce
218 anomaly (Fig. 2a). The curvature of some of the patterns ~~explains mostly~~ is largely responsible
219 for this range. In the Ce_{SN}/Ce_{SN}* vs. Pr_{SN}/Pr_{SN}* plot of Bau and Dulski (1996), where Ce* and
220 Pr* are linearly interpolated, only half of studied rock samples ~~is~~ are located in the panel
221 attributed to samples having no Ce and La anomalies; the other half being scattered in an area
222 corresponding to positive anomalies in Ce with either positive or negative La anomaly. This
223 discrepancy is somewhat surprising, as one would have expected the vast majority of studied

rocks to fall within the area corresponding to samples having no anomalies. This can be explained by the fact that the rocks used in our database display a much greater LREE compositional range relative to those used by Bau and Dulski (1996).

Next, we use Ce/Nd vs. Pr/Nd plots to compare linear or semi log extrapolations for Ce, normalizing ratios to either chondritic (Fig. 3a) or PAAS values (Fig. 3b). Indeed, the Ce^{*g}/Nd and Ce^{*l}/Nd ratios define parabolas and straight lines in these plots, respectively:

$$Ce_{CI}^{*g}/Nd_{CI} = (Pr_{CI}/Nd_{CI})^2 \text{ and } Ce_{SN}^{*g}/Nd_{SN} = (Pr_{SN}/Nd_{SN})^2 \quad (10)$$

$$Ce_{CI}^{*l}/Nd_{CI} = 2\,(Pr_{CI}/Nd_{CI}) - 1 \text{ and } Ce_{SN}^{*l}/Nd_{SN} = 2\,(Pr_{SN}/Nd_{SN}) - 1 \quad (11)$$

In eq. 10 and 11, I just removed some extra spaces.

The rocks of our database having no Ce anomaly, they can be directly compared to these curves or lines. Figure 3 shows directly that the parabolas calculated using a geometric extrapolation reproduce very satisfactorily the Ce/Nd ratios of the rocks over the whole range of Pr/Nd ratios considered in this study. On the other hand, the lines corresponding to the linear extrapolation allow for an acceptable approximation of Ce* in a given range of values only. Note that in each diagram the parabola and the line are tangent to the point (1,1). If we consider that both interpolations give acceptable results when Ce^{*g}/Ce^{*l} is between 1 and 1.05, we can easily calculate that we can then use indifferently one or the other extrapolation only when $(Pr/Nd)_{CI}$ or $(Pr/Nd)_{SN}$ are between 0.82 and 1.28. Whenever $(Pr/Nd)_{CI}$ or $(Pr/Nd)_{SN}$ plot outside this range of values, the Ce/Ce^{*l} and Ce/Ce^{*g} ratios diverge, due to a clear underestimation of Ce^{*l}. The choice of normalization values is not without consequence if linear extrapolation is used. The use of shales instead of chondritic reference values results in a shift towards the left of the diagram [because $(Pr/Nd)_{SN}<(Pr/Nd)_{CI}$], and, as a consequence, the Ce_{CI}/Ce_{CI}^{*l} and Ce_{SN}/Ce_{SN}^{*l} ratios may be very different depending on the Pr/Nd ratios. In this study, this is strikingly illustrated by the fact that the Ce_{CI}/Ce_{CI}^{*l} ratio varies from 0.91 to 1.24 only, while Ce_{SN}/Ce_{SN}^{*l} varies from 0.96 to 5.11. On the other hand, the Ce_{SN}/Ce_{SN}^{*g} and Ce_{CI}/Ce_{CI}^{*g} ratios are perfectly proportional, with $(Ce_{SN}/Ce_{SN}^{*g})/(Ce_{CI}/Ce_{CI}^{*g})$ being equal to the PAAS Ce_{CI}/Ce_{CI}^{*g} ratio.

In Fig. 4, we show the Ce/Ce^{*g} and Ce/Ce^{*l} ratios obtained after normalization to either chondritic or PAAS values. The diagrams not only indicate that the ranges of values obtained are different, but that the correlations are poor: Ce anomalies calculated in different ways are not comparable.

We followed the same approach for La anomalies. In La/Nd vs. Pr/Nd plots, the La^{*g}/Nd and La^{*l}/Nd ratios define cubic curves and straight lines, respectively:

$$La_{CI}^{*g}/Nd_{CI} = (Pr_{CI}/Nd_{CI})^3 \text{ and } La_{SN}^{*g}/Nd_{SN} = (Pr_{SN}/Nd_{SN})^3 \quad (12)$$

$$La_{CI}^{*l}/Nd_{CI} = 3\,(Pr_{CI}/Nd_{CI}) - 2 \text{ and } La_{SN}^{*l}/Nd_{SN} = 3\,(Pr_{SN}/Nd_{SN}) - 2 \quad (13)$$

As shown above, the curves corresponding to the geometric extrapolation superimpose well on the correlation trends displayed by the rock data used in this study (Fig. 5). The straight lines corresponding to the linear extrapolation only allow a good estimation of the La/Nd ratios for the patterns exhibit little REE decoupling (i.e., when $(Pr/Nd)_{CI}$ or $(Pr/Nd)_{SN}$ close to 1). Calculation of La anomalies using the linear extrapolation even appears to be inconsistent for many samples. When the data are normalized to chondritic reference values, the linear extrapolation underestimates considerably La* values, leading to anomalously high La/La^{*l} ratios. The situation is much more problematic when data are normalized to PAAS values, especially for the most light-REE depleted samples. Not only does Equation 8 underestimate La_{SN}^*, but when $(Pr/Nd)_{SN} \leq 2/3$, $La_{SN}^{*l} \leq 0$ and the La_{SN}/La_{SN}^{*l} ratio becomes negative or tends toward $-\infty$ when $(Pr/Nd)_{SN}$ is just below 2/3. The La_{SN}/La_{SN}^{*l} ratio also tends toward $+\infty$ when $(Pr/Nd)_{SN}$ is just above 2/3. These cases are not uncommon on Earth: the La_{SN}/La_{SN}^{*l} ratios calculated with our database range from -216.3 to 103.5, while much smaller ranges around 1 are obtained with other La/La* calculations (Fig. 6). As for the Ce anomaly, the ratios La_{SN}/La_{SN}^{*g} and La_{CI}/La_{CI}^{*g} are perfectly proportional, and the La/La^{*g} and La/La^{*l} ratios are not strongly correlated, even when the latter ratios are not aberrant. The range of $(Pr/Nd)_{SN}$ ratios for which La anomaly calculations are similar for linear or geometric interpolations ($La^{*g}/La^{*l}<1.05$) is narrow and only between 0.9 and 1.16.

These results demonstrate that La and Ce anomalies calculated using linear extrapolation can lead to biased or even aberrant values in many cases. Moreover, the calculated anomalies are very dependent on the type of normalization used. On the other hand, the results obtained with our database indicate that the use of geometric extrapolation results in more reliable estimates of La and Ce anomalies, ~~whatever~~ regardless of whether chondrite or shale are used for normalization, and this applies for the whole range of compositions tested in this study.

3/ Some examples

The theoretical ground discussed above is illustrated below for a few examples taken from the literature (Table 1). It is not our goal here to discuss the differences obtained between the anomalies calculated for each type of rocks or waters, normalizations and extrapolations. We have chosen to discuss in more detail the ~~case study~~ specific cases of seawater ~~samples~~ and biogenic carbonates~~,~~ in order to show how the choice of extrapolation can affect data interpretation.

3.1. Carbonates

We selected 5 series of carbonate samples corresponding to microbialites or stromatolites of different ages: the 3.45-Ga-old Strelley Pool stromatolites (Van Kranendonk et al., 2003); the 2.84-Ga-old Mushandike stromatolites (Kamber et al, 2004); the 2.52-Ga-old Campbellrand stromatolites (Kamber and Webb, 2001); the late Devonian reefal carbonates from the Lennard Shelf (Nothdurft et al., 2004); and the Holocene microbialites from the Heron Reef (Webb and Kamber, 2000). All data used here were obtained in the same laboratory (ACQUIRE, Brisbane) following similar analytical procedures, and are of excellent quality. These series of samples do not of course cover the full compositional range existing for ~~such~~ these types of carbonates, but nevertheless display important variations in various REE signatures.

We plotted these analyses in the Ce/Ce* vs. Pr/Pr* diagram of Bau and Dulski (1996a), which can be used, as discussed above, to identify the presence of Ce and La anomalies (Fig. 7a). In this diagram, Ce* and Pr* are linearly interpolated between La and Pr and Ce and Nd respectively. All but 2 samples have a Ce/Ce* ratio<1 when calculated in ~~that~~ this way, but only those with a Pr/Pr* ratio >1 have a true negative Ce anomaly, due to the bias introduced by the La anomalies. We calculated the Ce and La anomalies using both geometrical and linear extrapolation from PAAS-normalized concentrations. The obtained Ce_{SN}/Ce_{SN}^{*g} and Ce_{SN}/Ce_{SN}^{*l} ratios are very similar (Fig. 8a) for most samples. Only 4 samples from Strelley Pool deviate significantly from the trend, their Ce_{SN}^{*l} certainly being underestimated. The La_{SN}/La_{SN}^{*g} and La_{SN}/La_{SN}^{*l} ratios are for most samples reasonably well correlated, but the Holocene samples markedly deviate from the trend with La_{SN}/La_{SN}^{*l} ratios greater than La^{SN}/La_{SN}^{*g}, and 4 Strelley Pool samples display outlier La_{SN}/La_{SN}^{*l} values (=-27.7 to -4.6). These calculations show that in many cases, one can use either linear or geometric extrapolations to estimate La or Ce anomalies, without detecting an anomaly. This is

particularly the case when the patterns are little or not fractionated, but linear extrapolation can nevertheless generate artifacts or even aberrant values. To avoid the latter, we recommend using only the geometrical extrapolation to calculate La or Ce anomalies.

Although the Ce/Ce* vs. Pr/Pr* diagram proposed by Bau and Dulski (1996a) can bring useful insights for discussing REE patterns and the origin of La and Ce anomalies, it also suffers from inherent drawbacks that are briefly described below:

- The Ce/Ce* ratio used in this diagram depends on a Ce* value linearly interpolated between La and Pr. This ratio does not allow a correct quantification of the anomaly, because in addition to the problems related to the linear interpolation, it can be largely biased for the samples with an anomaly in La, as already reported by these authors

- the Pr/Pr* ratio allows for the detection of samples with positive or negative anomalies in La, but ~~the diagram~~ does not allow the quantification of the latter.

For all the above-mentioned reasons, we propose using instead the Ce/Ce^{*g} vs. La/La^{*g} diagram, which is ~~best~~ better suited for illustrating whether any given sample displays La or Ce anomalies, and which also provides direct quantification of these anomalies. Additionally, the use of the geometric extrapolation ensures that calculated anomalies in this diagram are independent of the type of reference used for normalization, ~~but~~ and above all it avoids the calculation of erroneous Ce/Ce* or La/La* ratios due to artifacts linked to linear extrapolation. For the carbonate samples selected here, the Ce/Ce^{*g} vs. La/La^{*g} diagram shows that these carbonates exhibit a wide range of positive La anomalies, but also allows one to identify a clear distinction between those Archean samples characterized by the absence of marked negative Ce anomalies ($Ce/Ce^{*g} \geq 1$), in contrast with the Devonian or Holocene carbonates.

3.2. Seawater

We employ ~~used~~ here a previously published REE database for seawater samples (n=1649; Bayon et al., 2020b). We normalized the concentrations with PAAS and examined ~~reported~~ $(Ce/Nd)_{SN}$ and $(La/Nd)_{SN}$ vs. $(Pr/Nd)_{SN}$ ~~plots~~ systematics (Fig. 9). The $(Pr/Nd)_{SN}$ ratios range from 0.49 to 1.19: 62% of the analyses have $(Pr/Nd)_{SN}$ ratios <0.82, and thus have Ce/Ce^{*l} and Ce/Ce^{*g} ratios that differ by more than 5%; 97% of the analyses have $(Pr/Nd)_{SN}$ ratios<0.9, and thus have La/La^{*l} and La/La^{*g} ratios that differ by more than 5%. The position of the points with respect to the calculated curves and lines shows unambiguously that the choice of

the extrapolation method is critical here, as the La^{*l} or Ce^{*l} concentrations are most often underestimated by the calculation, or even aberrant ($La^{*l}<0$ for many samples).

In order to illustrate the pitfalls of using the linear extrapolation for the case of seawater samples, we chose two hydrographic stations from the China Sea (Alibo and Nozaki, 2000) and the Kerguelen Plateau (Grenier et al., 2018), and ~~calculated~~ examined the vertical profiles of La anomalies calculated by normalizing the data with respect to both CI-chondrite and PAAS, extrapolating La* linearly or geometrically (Fig. 10). For both stations, La_{SN}/La_{SN}^{*l} ratios are always much larger than those estimated geometrically by normalizing with PAAS or with CI-chondrite: for the first station, La_{SN}/La_{SN}^{*l} ratios are 1.30 to 1.42 times larger than La_{SN}/La_{SN}^{*g} ratios, and for the second station they are 1.54 to 3.71 times larger. The La anomalies estimated with the La_{SN}/La_{SN}^{*l} ratios are obviously strongly exaggerated, and these calculations must be rejected. Note that the La_{CI}/La_{CI}^{*l} ratios are very close to the La_{CI}/La_{CI}^{*g} or La_{SN}/La_{SN}^{*g} ratios, and similar or identical profiles are obtained with these three ratios. These results adds further support that the use of geometric extrapolation is best suited for calculating La and Ce anomalies relative to the linear extrapolation. The fact that the La_{CI}/La_{CI}^{*l} ratios are correct here is fortuitous, and is easily explained. The $(Pr/Nd)_{CI}$ ratios are higher than the $(Pr/Nd)_{SN}$ ratios, and are then in the range of values for which geometric and linear extrapolations give equivalent results.

4/ Conclusion

An extended REE database for a suite of igneous rocks devoid of La and Ce anomalies, was used to investigate the effects of linear and geometric extrapolations for calculating La/La* and Ce/Ce* ratios in geological and environmental samples, based on Pr and Nd concentrations. We show that the linear extrapolation only provides reliable estimates of La* and Ce* for a limited range of REE compositions. These calculations can lead in many cases to biased La/La* and Ce/Ce* values, which are also critically dependent on the type of normalization used (i.e. chondritic versus shale reference values). The artifacts generated when using the linear extrapolation are illustrated with examples from the literature for seawater and biogenic carbonates, demonstrating that it can lead to misleading interpretations regarding the presence and/or significance of La and Ce anomalies. Finally, we show that the use of geometric extrapolation ensures reliable quantitative calculation of Ce and La anomalies in all samples, which remain unaffected by the type of normalization used. We propose that linear

extrapolations be discontinued ~~here~~, and instead recommend the exclusive use of geometric extrapolations to quantify La and Ce anomalies.

Acknowledgements.

We thank X for the editorial handling, and Y_1, Y_2, Y_{i+1} for their constructive reviews.

References

Alibo, D.S., Nozaki, Y. (2000) Dissolved rare earth elements in the South China Sea: geochemical characterization of the water masses. *J. Geophys. Res.* 105, C12, 28771-28783.

Anders E. and Grevesse N. (1989) Abundances of the elements: meteoritic and solar. *Geochim. Cosmochim. Acta* **53**, 197–214.

Barrat J.A., Zanda B., Moynier F., Bollinger C., Liorzou C., and Bayon G. (2012) Geochemistry of CI chondrites: Major and trace elements, and Cu and Zn isotopes. *Geochim. Cosmochim. Acta* **83**, 79-92.

Barrat J.A., Dauphas N., Gillet P., Bollinger C., Etoubleau J., Bischoff A., Yamaguchi A. (2016) Evidence from Tm anomalies for non-CI refractory lithophile element proportions in terrestrial planets and achondrites. *Geochim. Cosmochim. Acta*, **176**, 1-17.

Barrat J.A., Bayon G., Wang X., Le Goff S., Rouget M.L., Gueguen B., Ben Salem B. (2020) A new chemical separation procedure for the determination of rare earth elements and yttrium abundances in carbonates by ICP-MS. *Talanta* **219**, 121244.

Bau, M., Dulski, P. (1996a) Distribution of yttrium and rare-earth elements in the Penge and Kuruman iron formations, Transvaal Supergroup, South Africa. *Precambrian Res*. **79**, 37–55.

Bau, M., Dulski, P. (1996b) Anthropogenic origin of positive gadolinium anomalies in river waters. *Earth Planet. Sci. Lett.* **143**, 245-255.

Bau M., Romer R.L., Lüders V., Dulski P. (2003) Tracing element sources of hydrothermal mineral deposits: REE and Y distribution and Sr-Nd-Pb isotopes in fluorite from MVT deposits in the Pennine Orefield, England. *Mineralium Deposita* **38**, 992-1008.

Bau M., Koschinsky A. (2009) Oxidative scavenging of cerium on hydrous Fe oxide: Evidence from the distribution of rare earth elements and yttrium between Fe oxides and Mn oxides in hydrogenetic ferromanganese crusts. *Geochem. J.* **43**, 37–47.

Bau M., Schmidt K., Pack A., Bendel B., Kraemer D. (2018) The European Shale: an improved data set for normalization of rare earth elements and yttrium concentrations in environmental and biological samples from Europe. *Applied Geochem.* **90**, 142-149.

Bayon G., Lambert T., Vigier N., De Dekker P., Freslon N., Jang K., Larkin C.S., Piotrovski A.M., Tachikawa K., Thollon M., Tipper E.D. (2020a) Rare earth element and neodymium isotope tracing of sedimentary rock weathering. *Chem. Geol.* **553**, 119794.

Bayon G., Lemaitre N., Barrat J.A., Wang X., Feng D., Duperron S. (2020b) Microbial utilization of rare earth elements at cold seeps related to aerobic methane oxidation. *Chem. Geol.* **555**, 119832.

Bellefroid E.J., Hood A.V.S. , Hoffman P.F., Thomas M.D., Reinhard C.T., Planavsky N.J. (2018) Constraints on Paleoproterozoic atmospheric oxygen levels. *PNAS* **115**, 8104-8109.

Bolhar R., Kamber B.S., Moorbath S., Fedo C.M., and Whitehouse, M.J. (2004). Characterisation of early Archaean chemical sediments by trace element signatures. *Earth Planet. Sci. Lett.* **222**, 43-60.

Burnham A.D., Berry A.J. (2012) An experimental study of trace element partitioning between zircon and melt as a function of oxygen fugacity. *Geochim. Cosmochim. Acta* **95**, 196-212.

Byrne R.H., Kim K.H. (1990) Rare earth element scavenging in seawater. *Geochim. Cosmochim. Acta* **54**, 2645-2656.

Byrne R.H., Liu X., and Schijf J. (1996). The influence of phosphate coprecipitation on rare earth distributions in natural waters. *Geochim. Cosmochim. Acta* **60**, 3341–3346.

Caroff M., Barrat J.A., Le Gall B. (2021) Kersantites and associated intrusives from the type locality (Kersanton), Variscan Belt of Western Armorica. *Gondwana Res.* **98**, 46-62.

Cordier C., Benoit M., Hémond C., Dyment J., Le Gall B., Briais A., Kitazawa M. (2010), Time scales of melt extraction revealed by distribution of lava composition across a ridge axis. *Geochem. Geophys. Geosyst.* **11**, Q0AC06,doi:10.1029/2010GC003074.

Charles C., Barrat J.A., Pelleter E. (2021) Trace element determinations in Fe–Mn oxides by high resolution ICP-MS after Tm addition. *Talanta* **233**, 122446.

Class C., Le Roex A.P. (2008) Ce anomalies in Gough Island lavas - Trace element characteristics of a recycled sediment component. *Earth Planet. Sci. Lett.* **265**, 475-486.

Coryell C.D., Chase J. W., and Winchester J.W. (1963) A procedure for geochemical interpretation of terrestrial rare-earth abundance patterns. *J. Geophys. Res.* **68**, 559-566

Cotruvo, jr., J.A. (2019) The chemistry of lanthanides in biology: recent discoveries, emerging principles, and technological applications. *ACS Cent. Sci.* 5, 1496−1506.

Daoud M.A., Maury R.C., Barrat J.A., Taylor R.N., Le Gall B., Guillou H., Cotten J., Rolet J. (2010) A LREE-depleted component in the Afar plume: further evidence from Quaternary Djibouti basalts. *Lithos* **114**, 327-336.

Dauphas N, Pourmand A. (2015) Thulium anomalies and rare earth element patterns in meteorites and Earth: Nebular fractionation and the nugget effect. *Geochim. Cosmochim. Acta* **163**, 234-261.

De Baar H.J.W., Bacon M.P., Brewer P.G. (1983) Rare-earth distributions with a positive Ce anomaly in the Western North Atlantic Ocean. *Nature* **301**, 324-327.

De Baar H.J.W., Bacon M.P., Brewer P.G., and Bruland, K.W. (1985) Rare earth elements in the Pacific and Atlantic oceans. *Geochim. Cosmochim. Acta* **49**, 1943–1959.

Elderfield H. (1988) The oceanic chemistry of the rare-earth elements. *Philosophical Transaction of the Royal Society of London. Series A, Mathematical and Physical Sciences* **325**, 105-126.

Elderfield H., and Greaves M.J. (1981) Negative cerium anomalies in the rare earth element patterns of oceanic ferromanganese nodules. *Earth Planet. Sci. Lett.* **55**, 163-170.

Elderfield H., Pagett R. (1986) Rare Earth elements in Ichthyoliths: variations with redox conditions and depositional environment. In: Riley, J.P. (Ed.), Science of the Total Environment. Elsevier, Amsterdam, pp. 175–197.

German C.R., Elderfield H. (1990) Application of the Ce anomaly as a paleoredox indicator: The ground rules. *Paleoceanography* **5**, 823-833.

German C.R., Holliday B.P., Elderfield H. (1991) Redox cycling of rare earth elements in the suboxic zone of the Black Sea. *Geochim. Cosmochim. Acta* **55**, 3553-3558.

Goldberg E.D., Koide M., Schmitt R.A. (1963) Rare earth distributions in the marine environment. *J. Geophys. Res.* **68**, 4209-4217.

Grenier M, Garcia-Solsona E., Lemaitre N., Trull T.W., Bouvier V., Nonnotte P., Van Beek P., Souhaut M., Lacan F., Jeandel C. (2018) Differentiating lithogenic supplies, water mass transport, and biological processes on and off the Kerguelen Plateau using rare earth element concentrations and neodymium isotopic compositions. *Frontiers in Marine Science* **5**, 426.

Hamelin C., Seitz H.M., Barrat J.A., Dosso L., Maury R.C., Chaussidon M. (2009) A low δ^7Li lower crustal component: evidence from an alkalic intraplate volcanic series (Chaîne des Puys, French Massif Central). *Chem. Geol.* **266**, 214-226.

Hamelin C., Dosso L., Hanan B., Barrat J.A., Klingelhöfer F., Ondréas H. (2010) Sr-Nd-Hf isotopes along the Pacific Antarctic Ridge from 41 to 53°S. *Geophys Res*. *Lett*. 37, L10303, doi:10.1029/2010GL042979.

Hein J. R., Zierenberg R. A., Maynard J. B., and Hannington, M. D. (2007). Multifarious barite-forming environments along a rifted continental margin, Southern California Borderland. Deep-Sea Res. II 54, 1327-1349.

Kamber B.S. and Webb G.E. (2001) The geochemistry of late Archaean microbial carbonate: Implications for ocean chemistry and continental erosion history. *Geochim. Cosmochim. Acta* **65,** 2509–2525.

Kamber B.S., Bolhar R., Webb G.E. (2004). Geochemistry of late Archaean stromatolites from Zimbabwe: evidence for microbial life in restricted epicontinental seas. *Precambrian Res.* **132**, 379-399.

Kulaksiz S., Bau M. (2007) Contrasting behaviour of anthropogenic gadolinium and natural rare earth elements in estuaries and the gadolinium input into the North Sea. *Earth Planet. Sci. Lett.* **260**, 361-371.

Kulaksiz S., Bau M. (2013) Anthropogenic dissolved and colloid/nanoparticle-bound samarium, lanthanum and gadolinium in the Rhine River and the impending destruction of the natural rare earth element distribution in rivers. *Earth Planet. Sci. Lett.* **362**, 43-50.

Lawrence M.G., Greig A., Collerson K.D., Kamber B.S. (2006) Rare Earth Element and Yttrium variability in South East QueenslandWaterways. *Aquat. Geochem.* **12**, 39–72.

Le Goff S., Barrat J.A., Chauvaud L., Paulet Y.M., Gueguen B., Ben Salem D. (2019) Compound-specific recording of gadolinium pollution in coastal waters by great scallops. *Scientific Reports* **9**, 8015.

Ma L., Dang D.H., Wang W., Evans R.D., Wang W.X. (2019) Rare earth elements in the Pearl River Delta of China: Potential impacts of the REE industry on water, suspended particles and oysters. *Environmental Pollution* **244**, 190-201

Masuda A. (1962) Regularities in variation of relative abundances of Lanthanide elements and an attempt to analyse separation index patterns of some minerals. *J. Earth Sci. Nagoya Univ.* **10**, 173-187.

Merschel G., Bau M. (2015) Rare earth elements in the aragonitic shell of freshwater mussel Corbicula fluminea and the bioavailability of anthropogenic lanthanum, samarium and gadolinium in river water. *Sci. Total Environment* **533**, 91-101.

Nance W.B., Taylor S.R., (1976) Rare earth element patterns and crustal evolution–I. Australian post-Archean sedimentary rocks. *Geochim. Cosmochim. Acta* **40**, 1539–1551.

Northdurft L.D., Webb G.E., Kamber B.S. (2004) Rare earth element geochemistry of Late Devonian reefal carbonates, Canning Basin, Western Australia: confirmation of a seawater REE proxy in ancient limestones *Geochim. Cosmochim. Acta* **68**, 263-283.

Palme H., Lodders K. and Jones A. (2014) Solar System Abundances of the Elements. In: Holland H.D. and Turekian K.K. (eds.) Treatise on Geochemistry, Second Edition, vol. 2, pp. 15-36. Oxford: Elsevier.

Piper D.Z. (1974a) Rare earth elements in the sedimentary cycle: a summary. *Chem. Geol.* **14**, 285--304.

Piper D.Z. (1974b) Rare earth elements in ferromanganese nodules and other marine phases. *Geochim. Cosmochim. Acta* **38**, 1007–1022.

Pelleter A.A., Caroff M., Cordier C., Bachelery P., Nehlig P., Debeuf D., Arnaud N. (2014) Melilite-bearing lavas in Mayotte (France): An insight into the mantle source below the Comores. *Lithos* **208-209**, 281-297.

Pol, A. *et al*. (2014) Rare earth metals are essential for methanotrophic life in volcanic mudpots. *Environmental Microbiology* **16**, 255–264.

554 Pourmand, A., Dauphas, N., Ireland, T.J. (2012) A novel extraction chromatography and MC-ICP-MS technique
555 for rapid analysis of REE, Sc and Y: Revising CI-chondrite and Post-Archean Australian Shale (PAAS)
556 abundances. *Chem. Geol.* **291**, 38-54.
557
558 Semrau, J.D., DiSpirito, A.A., Gu, W., Yoon, S. (2018) Metals and Methanotrophy. *Appl Environ Microbiol* **84**,
559 e02289-17.
560
561 Shimizu H., Sawatari H., Kawata Y., Dunkley P.N., Masuda A. (1992) Ce and Nd isotope geochemistry on island
562 arc volcanic rocks with negative Ce anomaly: existence of sources with concave REE patterns in the mantle
563 beneath the Solomon and Bonin island arcs. *Contrib. Mineral. Petrol.* **110**, 242-252.
564
565 Smythe D.J., Brenan J.M. (2016) Magmatic oxygen fugacity estimated using zircon-melt partitioning of cerium.
566 *Earth Planet. Sci. Lett*. **453**, 260-266.
567
568 Toyoda K., Nakamura Y., Masuda A., 1990. Rare earth elements of Pacific pelagic sediments. *Geochim.*
569 *Cosmochim. Acta* **54**, 1093–1103.
570
571 Tostevin R., Graham A., Shields G.A., Tarbuck G.M., Tianchen He, Clarkson M.O., Wood R.A. (2016) Effective
572 use of cerium anomalies as a redox proxy in carbonate-dominated marine settings. *Chem. Geol.* **438**, 146-
573 162
574
575 Trail D., Watson E.B., Tailby N.D. (2012) Ce and Eu anomalies in zircon as proxies for the oxidation state of
576 magmas. *Geochim. Cosmochim. Acta* **97**, 70-87.
577
578 Valdés-Vilchis S., Sànchez-Beristain F., Bernal J.P., Juàrez-Aguilar E.A. (2021) Rare Earth Elements and Yttrium
579 (REE+Y) patterns in recent *Anadara brasiliana* shells from Playa Norte, Barra de Cazones (Veracruz,
580 Mexico): Evidence of anthropogenic contamination linked to river output? *Journal of South American Earth*
581 *Sciences* **110**, 103368.
582
583 Van Kranendonk M.J., Webb G.E., Kamber B.S. (2003) New geological and trace element evidence from 3.45 Ga
584 stromatolitic carbonates in the Pilbara Craton: support of a marine, biogenic origin and for a reducing
585 Archaean ocean. *Geobiology* **1**, 91-108.
586
587 Wallace M.W., Hood A.S., Shuster A., Greig A., Planavsky N.J., Reed C.P. (2017) Oxygenation history of the
588 Neoproterozoic to early Phanerozoic and the rise of land plants. *Earth Planet. Sci. Lett.* **466**, 12-19.
589
590 Wang X., Barrat J.A., Bayon G., Chauvaud L., Feng D. (2020) Lanthanum anomalies as fingerprints of
591 methanotrophy. *Geochem. Persp. Let.* **14**, 26–30.
592
593 Webb G.E., Kamber B.S. (2000) Rare earth elements in Holocene reefal microbialites: a new shallow seawater
594 proxy. *Geochim. Cosmochim. Acta* **64**, 1557-1565.
595

Table 1. Preferred normalization values and examples of calculation. (References: 1: Barrat et al., 2012; 2: Pourmand et al., 2012; 3: Barrat et al., 2016 ; 4 : Bau et al., 2003 ; 5 : Charles et al., 2021 ; 6 : Van Kranendonk et al., 2003).

	CI-chondrite	CI-chondrite	PAAS	PAAS	MORB	fluorite	Mn-nodule	stromatolite	BIF
ref.	1	1	2	2	3	4	5	6	6
#					PI 18-06	CT2a	GSMC-1	2-9-11a	IF-G
unit	µg/g	µmol/kg	µg/g	µmol/kg	µg/g	µg/g	µg/g	ng/g	ng/g
Y	1.56	17.55	32.2	362		35.6	259	1014.2	9135
La	0.235	1.692	44.75	322.2	0.504	0.54	326	56.3	2706
Ce	0.600	4.28	87.29	623.0	2.13	0.89	1246	85.9	3902
Pr	0.091	0.646	10.1	71.68	0.464	0.23	68.74	14	430
Nd	0.464	3.22	36.98	256.4	3.00	1.42	283	77.7	1731
Sm	0.153	1.018	6.908	45.94	1.30	0.57	58.4	45.9	399
Eu	0.0586	0.386	1.188	7.818	0.582	0.18	14.36	27.1	362
Gd	0.206	1.31	5.958	37.89	2.18	1.33	61.68	89.6	667
Tb	0.0375	0.236	0.894	5.625	0.432	0.23	9.53	13.6	112
Dy	0.254	1.563	5.272	32.44	3.16	1.71	56.48	70	791
Ho	0.0566	0.343	1.078	6.536	0.743	0.4	11.58	17.7	207
Er	0.166	0.992	3.094	18.50	2.23	1.15	31.93	54.8	619
Tm	0.0262	0.155	0.468	2.770		0.13			
Yb	0.168	0.971	3.028	17.50	2.28	0.61	29.2	48	580
Lu	0.0246	0.141	0.438	2.503	0.34	0.07	4.26	8.6	90.4
La_{CI}/La_{CI}* [g]	1	1	0.88	0.88	0.68	1.33	1.20	1.84	1.52
Ce_{CI}/Ce_{CI}* [g]	1	1	0.94	0.94	0.88	0.71	2.22	1.01	1.09
La_{CI}/La_{CI}* [1]	1	1	1.10	1.10	0.91	1.57	1.33	1.89	1.71
Ce_{CI}/Ce_{CI}* [1]	1	1	1.02	1.02	0.95	0.74	2.31	1.02	1.14
La_{SN}/La_{SN}* [g]	1.13	1.13	1	1	0.76	1.51	1.35	2.09	1.72
Ce_{SN}/Ce_{SN}* [g]	1.06	1.06	1	1	0.94	0.75	2.36	1.08	1.15
La_{SN}/La_{SN}* [1]	2.71	2.71	1	1	-0.46	-1.42	1.42	-28.69	1.77
Ce_{SN}/Ce_{SN}* [1]	1.26	1.26	1	1	2.27	1.43	2.40	1.47	1.17

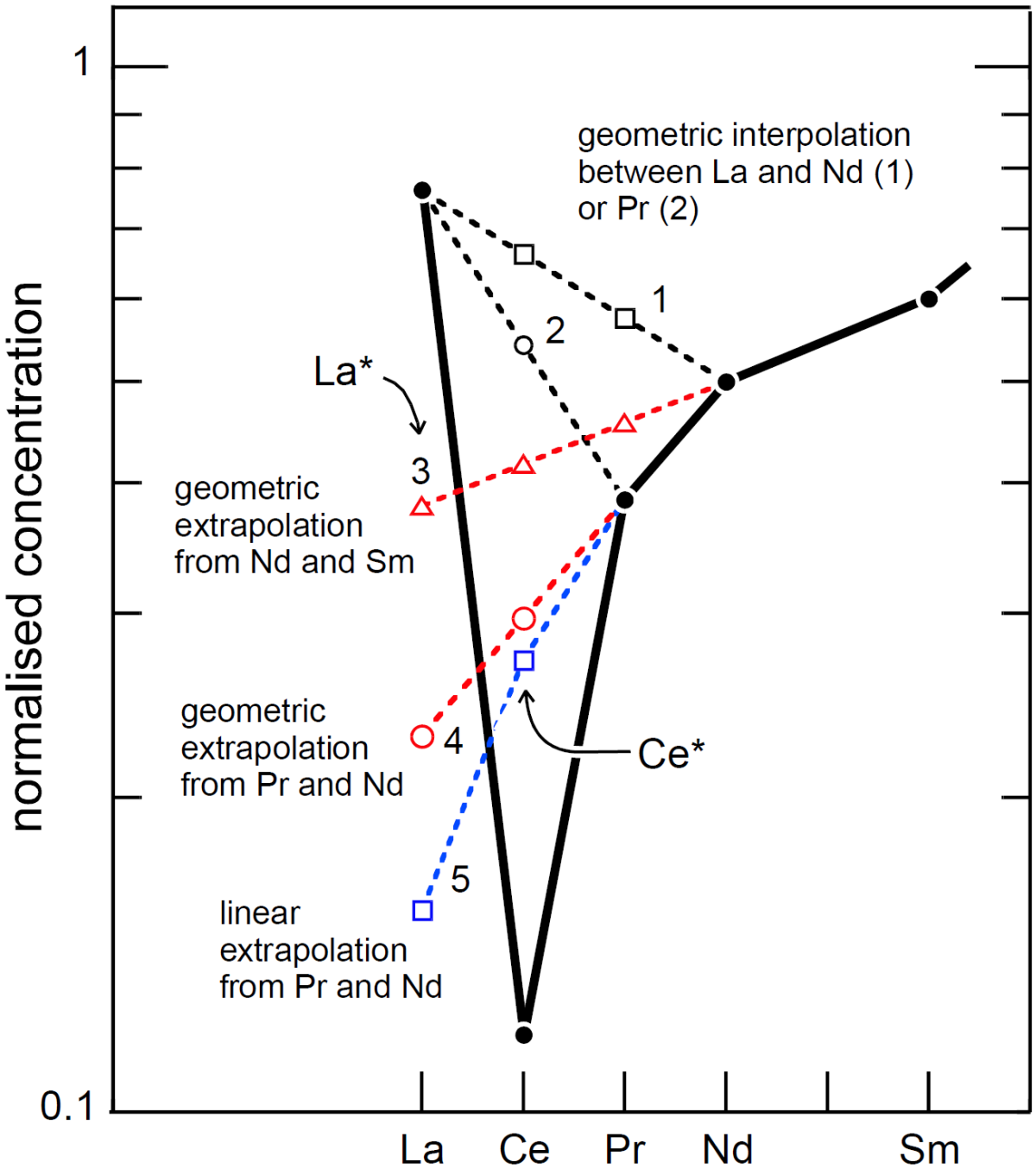

Figure 1. The different ways of calculating La* and Ce*.

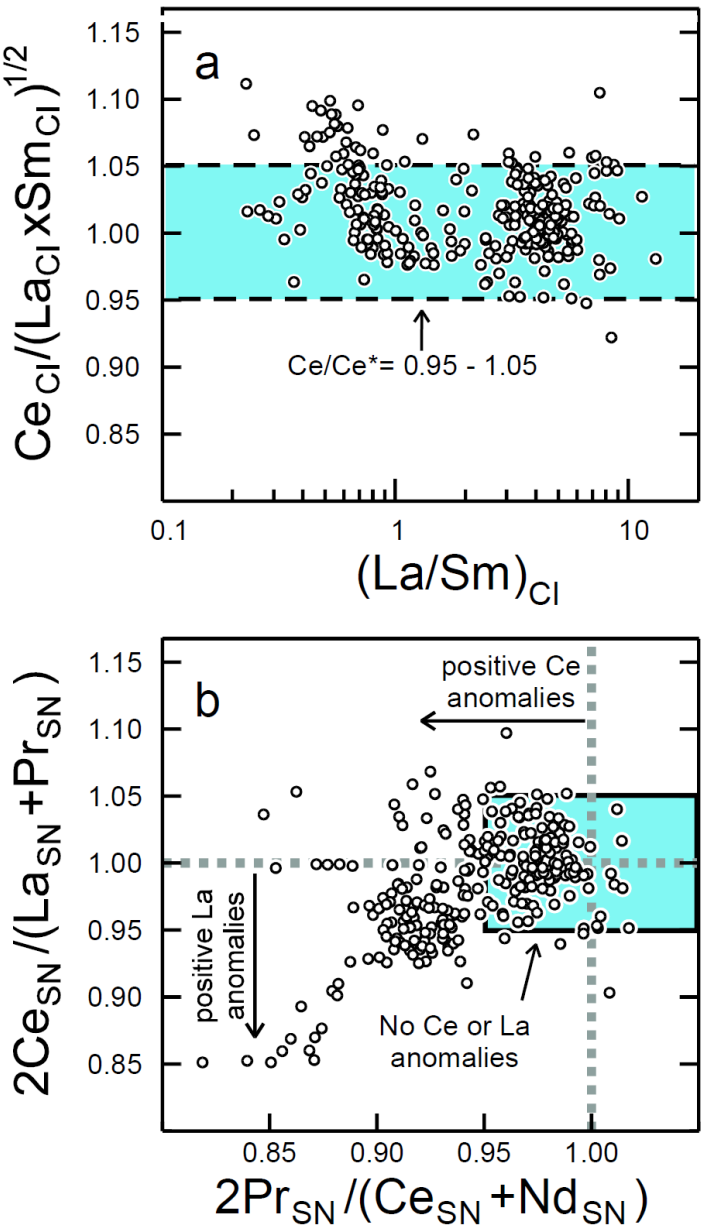

Figure 2. The 286 samples devoid of true La and Ce anomalies of the database used to compare linear and geometric extrapolations for calculating La* and Ce*, are plotted in a Ce/Ce* vs. La/Sm plot (a) and in the Ce/Ce* vs. Pr/Pr* plot of Bau and Dulski (1996a) (b). Ce* is geometrically interpolated in (a) and linearly interpolated in (b).

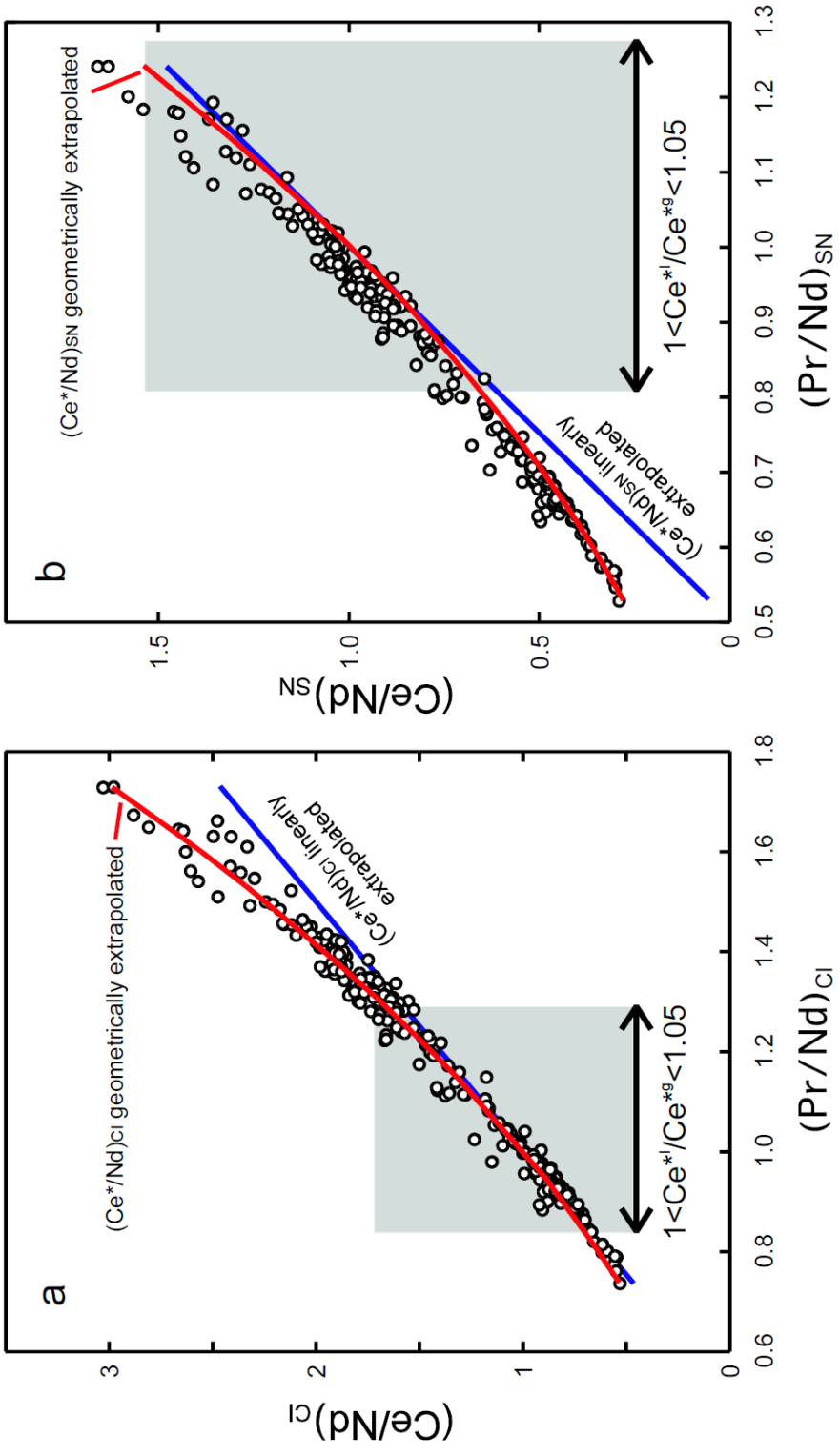

Figure 3. Ce/Nd vs. Pr/Nd plots for the samples devoid of true La and Ce anomalies of our database, used here to compare linear (blue line) and geometric (red parabola) extrapolations for Ce*. The data are normalized with CI chondrite (a) or with PAAS (b).

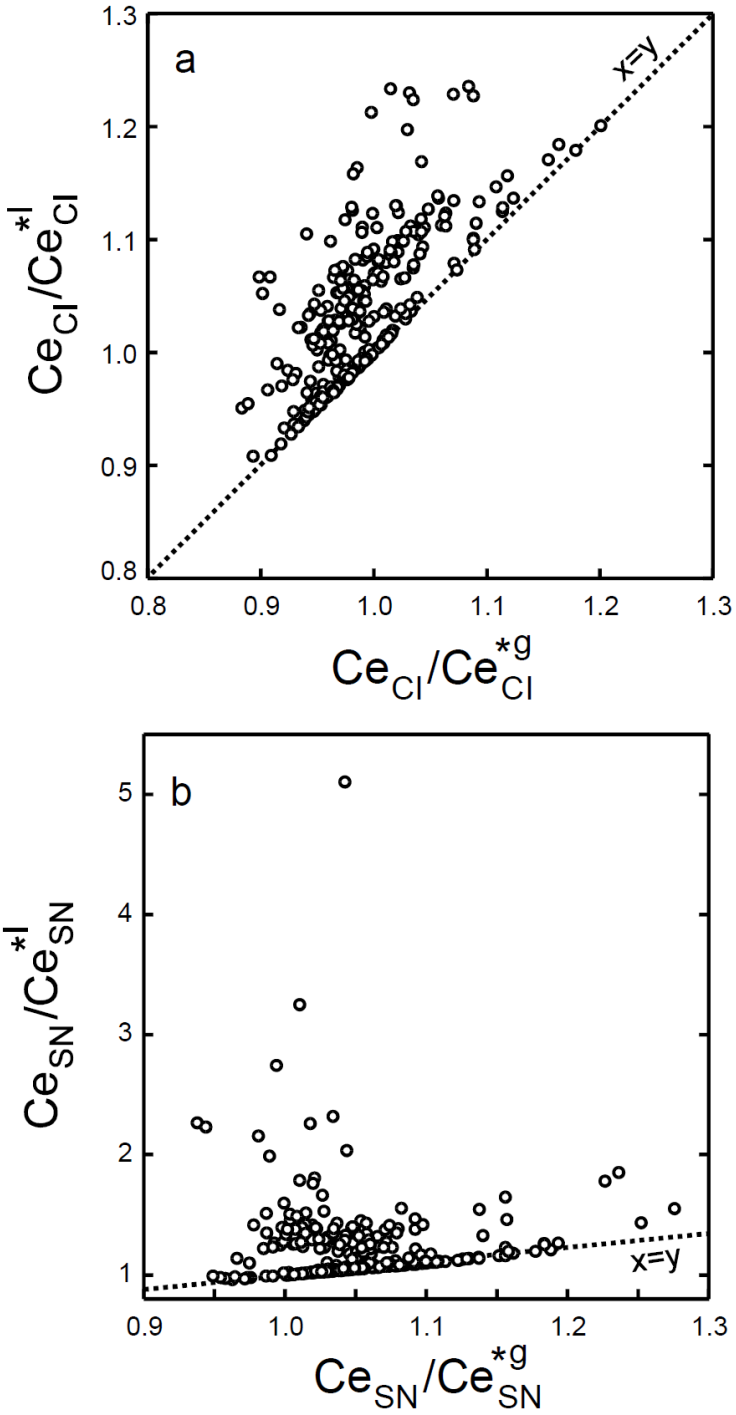

Figure 4. Ce_{CI}/Ce_{CI}^{*l} vs. Ce_{CI}/Ce_{CI}^{*g} (a) and Ce_{SN}/Ce_{SN}^{*l} vs. Ce_{SN}/Ce_{SN}^{*g} (b) plots for the samples devoid of true Ce anomalies used to test the different extrapolations. Notice the ranges of values obtained.

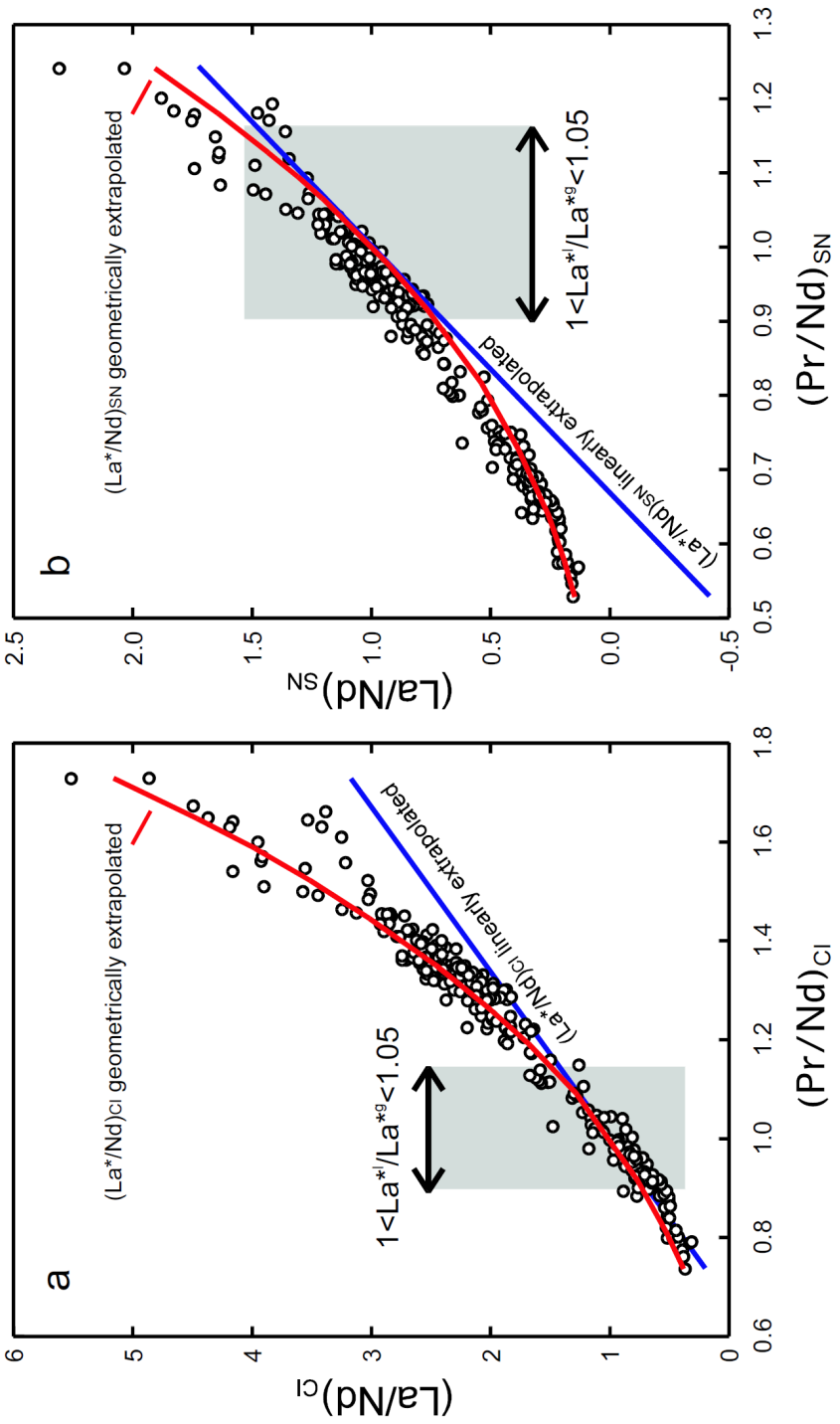

Figure 5. La/Nd vs. Pr/Nd plots for the samples devoid of true La and Ce anomalies of our database used to compare linear (blue line) and geometric (red cubic) extrapolations for Ce*. The data are normalized with CI chondrite (a) or with PAAS (b).

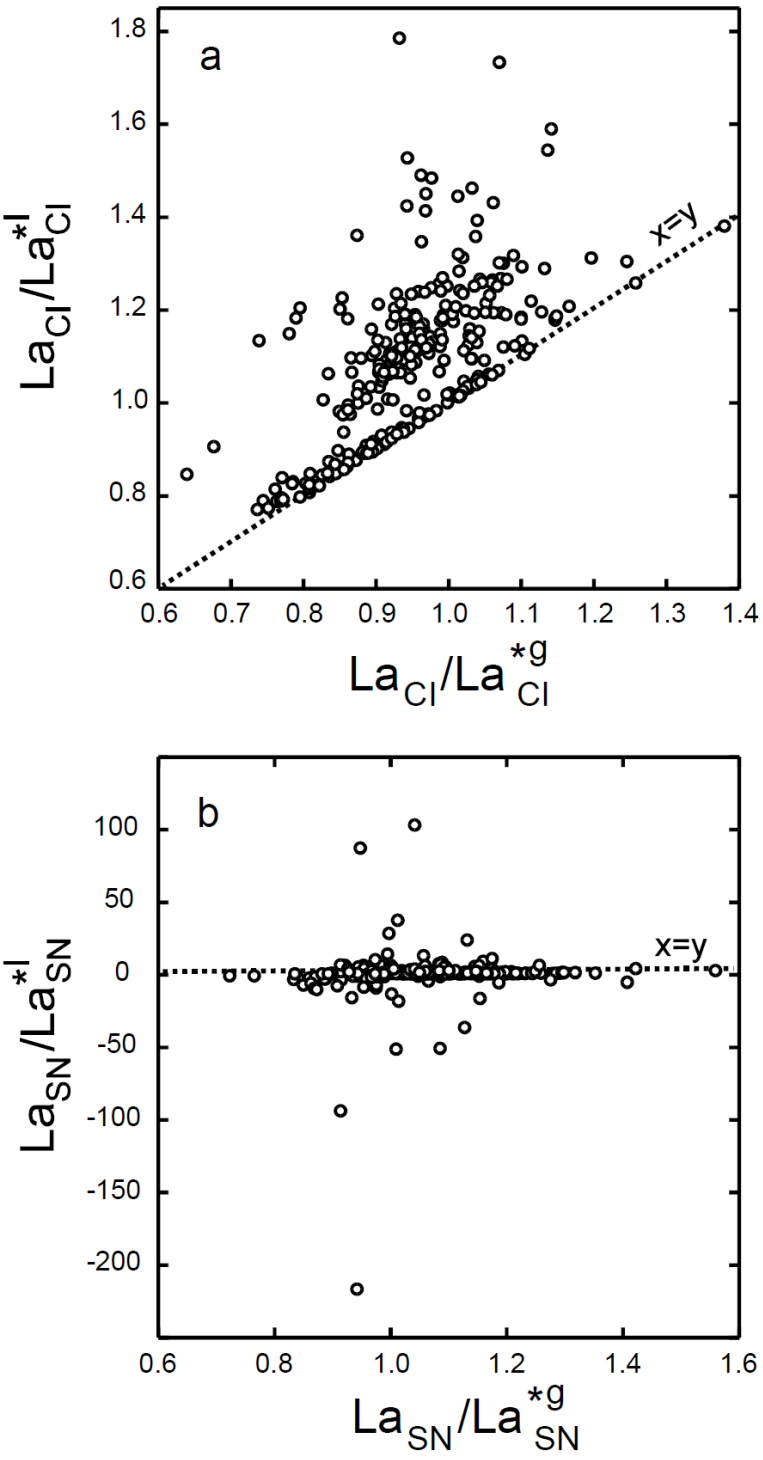

635

636 Figure 6. La_{CI}/La_{CI}^{*l} vs. La_{CI}/La_{CI}^{*g} (a) and La_{SN}/La_{SN}^{*l} vs. La_{SN}/La_{SN}^{*g} (b) plots for the
637 samples devoid of true La anomalies used to test the different extrapolations. Notice the ranges
638 of values obtained.

639

640

641

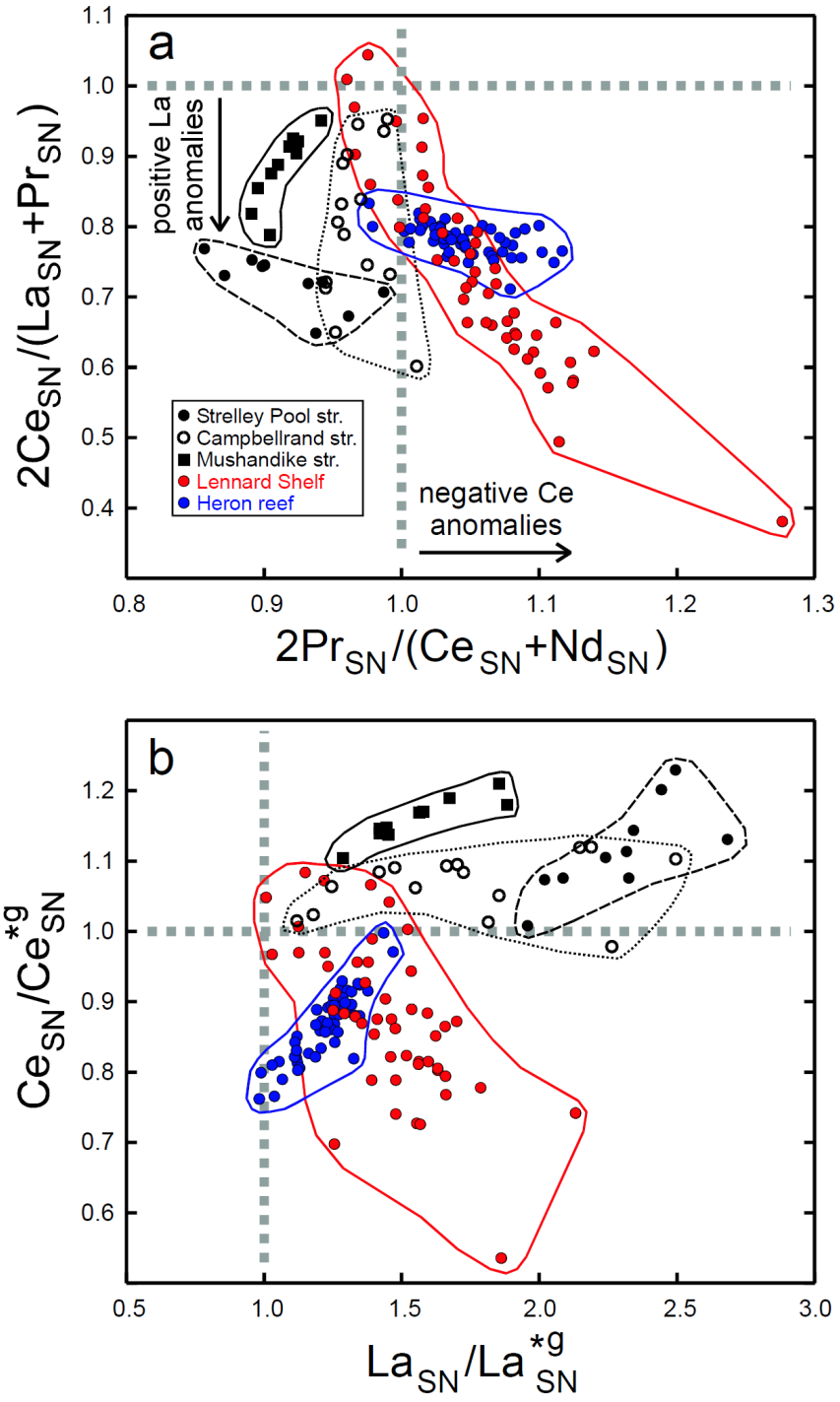

Figure 7. Selected carbonates are plotted in the Ce/Ce* vs. Pr/Pr* plot of Bau and Dulski (1996a) (a) where Ce* and Pr* are linearly interpolated, and in a Ce/Ce* vs. La/La* where Ce* and La* are geometrically interpolated. Notice the different Ce/Ce* ranges obtained. See text for more details.

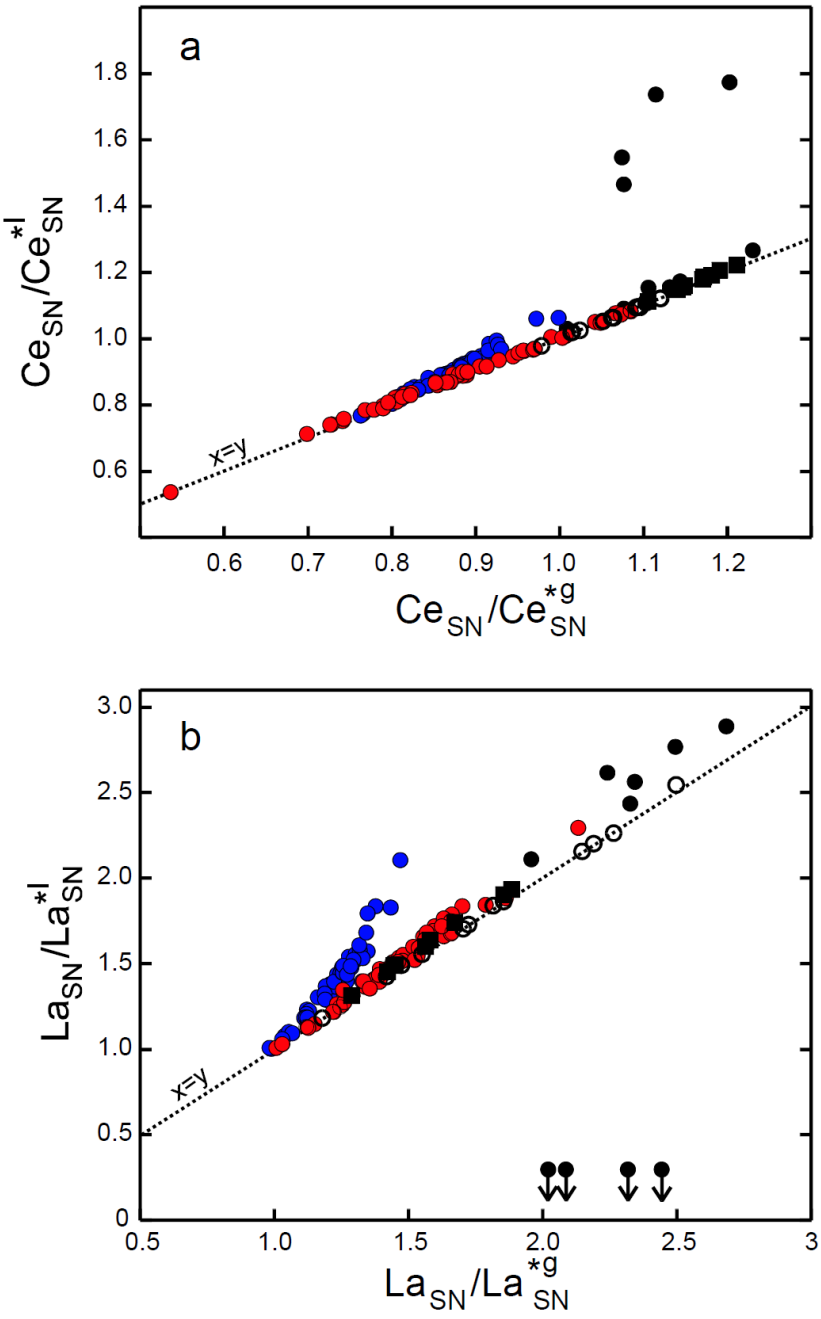

649

650 Figure 8. Ce_{SN}/Ce_{SN}^{*l} vs. Ce_{SN}/Ce_{SN}^{*g} (a) and La_{SN}/La_{SN}^{*l} vs. La_{SN}/La_{SN}^{*g} (b) plots for the
651 selected carbonates used to test the different extrapolations (same caption as Fig. 7).

652

653

654

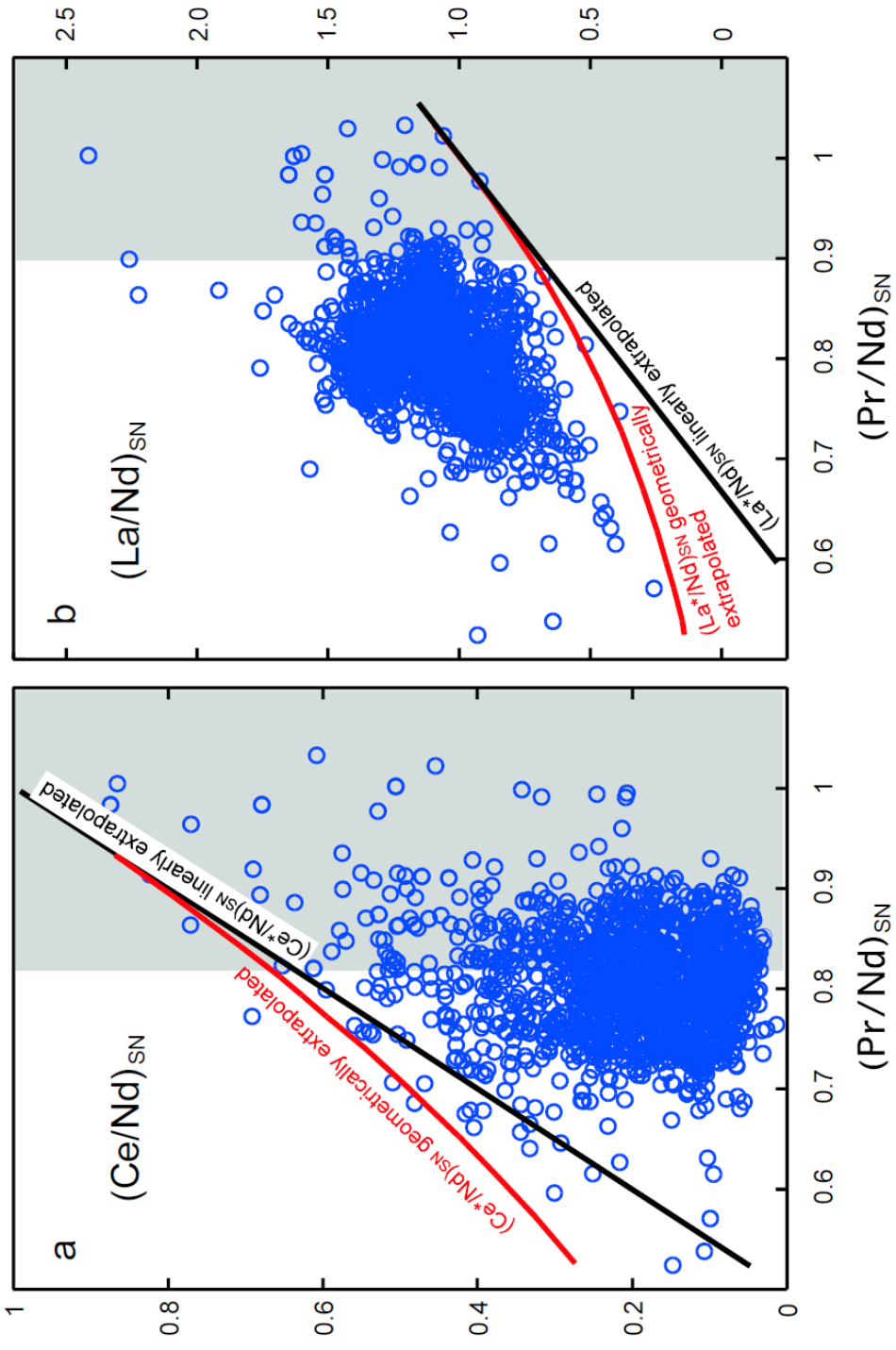

Figure 9. $(Ce/Nd)_{SN}$ (a) and $(La/Nd)_{SN}$ (b) vs. $(Pr/Nd)_{SN}$ plots for seawater. The shaded areas correspond to the range in Pr/Nd ratios for which the linear and geometric extrapolations are similar ($1<X^*l/X^*g<1.05$)~~, correspond to the areas that have been shaded~~. A large proportion of the samples are outside the ranges where the linearly extrapolated Ce* or La* are equivalent to the geometrically extrapolated ones.

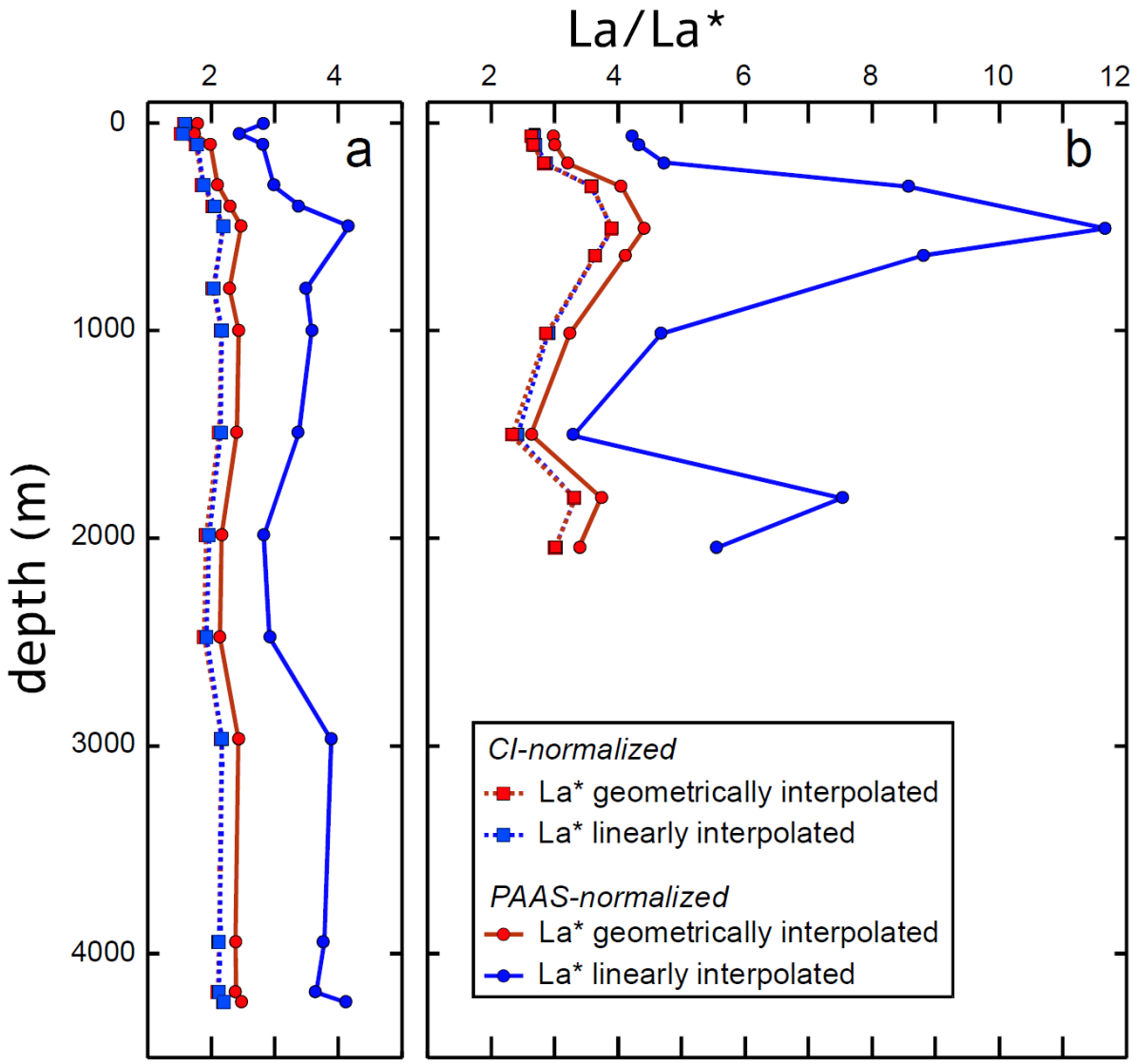

665

666 Figure 10. Vertical profiles of La anomaly (La/La*) at (a) station PA-11, South China Sea
667 (February 11 and 12, 1997; 15°22'N, 115°17'E; depth: 4240 m ; Alibo and Nozaki, 2000) and
668 at (b) the meander core station E1, Kerguelen Plateau (October 30, 2011; 72.178°E, 48.498°S;
669 depth: 2058 m, Grenier et al., 2018). La/La* was calculated linearly and geometrically with
670 data normalized with chondrite or with PAAS. The La_{SN}/La_{SN}^{*l} values are always much larger
671 than the other La/La* estimates, and is an artifact.